PAPER

Check for updates

Advanced 2D MoS$_2$–chitosan nanocomposites for ultra-sensitive and selective dopamine detection

Ratiba Wali,[a] Rayhane Zribi, [ID] *[bc] Viviana Bressi,[c] Ramzi Maalej, [ID] [a] Antonino Foti,[b] Pietro Giuseppe Gucciardi,[b] Wissem Cheikhrouhou-Koubaa[d] and Giovanni Neri [ID] [c]

Dopamine, an essential neurotransmitter in the central nervous system, plays a key role in neurological disorders such as Parkinson's disease, making its accurate monitoring critical for effective prevention, diagnosis, and management. This study introduces a novel and cost-effective electrochemical sensor for dopamine detection, leveraging molybdenum disulfide–chitosan (Cs–MoS$_2$) nanohybrids synthesized *via* a simple liquid-phase exfoliation (LPE) method. Chitosan nanoparticles were dispersed in a solution containing molybdenum disulfide (MoS$_2$) nanosheets to form the Cs–MoS$_2$ nanohybrids. These nano-hybrids were extensively characterized using UV-visible spectroscopy, Fourier transform infrared (FTIR) spectroscopy, Raman spectroscopy, thermogravimetric analysis (TGA), and atomic force microscopy (AFM), confirming their successful synthesis and unique properties. Commercial screen-printed electrodes (SPEs) were modified with the Cs–MoS$_2$ nanohybrids and evaluated for dopamine sensing through cyclic voltammetry (CV), electrochemical impedance spectroscopy (EIS), and differential pulse voltammetry (DPV). The sensor exhibited high sensitivity, with two distinct linear response ranges: 4.48 µA µM^{-1} cm^{-2} for 0–40 µM and 1.67 µA µM^{-1} cm^{-2} for 40–440 µM. The limit of detection (LOD) was determined to be 0.8 µM. These performance metrics demonstrate superior analytical capabilities, including excellent selectivity against common interfering species in body fluids, good stability, and reproducibility. The findings underline the novelty of utilizing Cs–MoS$_2$ nanohybrids in electrochemical dopamine detection and highlight their potential for practical applications in biomedical diagnostics.

1. Introduction

Researchers in the ever-advancing field of nanotechnology have acclaimed nanocomposites as ground-breaking materials defining the twenty-first century.[1] These remarkable materials are characterized by their dimensions within the nanoscale range.[1] Compared to conventional materials, nanocomposites exhibit unique properties surpassing their constituent elements.[2] This is attributed to their significantly higher surface-to-volume ratio, which leads to enhanced interactions. As a result, nanocomposites display distinctive physical, chemical, optical, mechanical, magnetic, and electrical characteristics.

Dopamine (DA) plays a crucial role in the functions of human beings and the determination of DA as an essential basis of clinical diagnosis has attracted much interest.[3,4] DA is a crucial

neurotransmitter that facilitates chemical signal transmission between cells.[5] Its brain secretion is intricately linked to human emotions, desires, and sensations, serving as a conduit for transmitting feelings of excitement and happiness.[6] Disruptions in dopamine's normal functioning in the human body can contribute to the development of various neurological disorders, including Parkinson's disease, Huntington's disease, and schizophrenia.[7] For these reasons, different methods have been used for DA analysis, including flow injection, chromatography, electrolysis, and chemiluminescence.[8] Since DA functions as a redox-active neurotransmitter, electrochemical techniques offer a practical solution for DA detection, due to their affordability, ease of miniaturization, and enhanced sensitivity. Consequently, electrochemical sensors have emerged as the standard choice, characterized by their low cost, rapid response time, and ability to integrate with circuits, facilitating accurate quantitative measurements.[9] However, the presence of other biologically relevant biomolecules, such as ascorbic acid, glucose, and uric acid, can significantly impact the selectivity and sensitivity of electrochemical sensors, thereby posing a challenge in accurately quantifying DA levels.[10] Numerous nanomaterials, including noble metal nanoparticles,[11] carbon nanotubes,[12] graphene and its derivatives,[13] metal–organic alloy nanoparticles,[14] and metal

a Laboratory of Ceramic Composite Materials and Polymers, Sciences Faculty of Sfax, University of Sfax, Tunisia

b CNR IPCF Istituto per i Processi Chimico-Fisici, viale F. Stagno D'Alcontres 37, I-98156 Messina, Italy

c Department of Engineering, University of Messina, C. da Di Dio, I-98166 Messina, Italy

d Centre de Recherche en Numérique de Sfax, Technopole of Sfax, BP 275, Sfax, 3021, Tunisia

oxides,[12] have been identified to exhibit enzyme-like activity.[15] The catalytic behaviour observed in 2D materials involves facilitating chemical reactions by providing reactive surfaces for molecular interactions, thereby reducing activation energy barriers, facilitating bond formation or cleavage, and improving reaction kinetics and selectivity.[15,16] These characteristics parallel the functional role of enzymes in biological systems.[15,16]

The catalytic activity exhibited by 2D materials involves facilitating chemical reactions by providing a surface for molecules to interact, lowering the activation energy barrier, promoting bond breaking or formation, and enhancing reaction rates and selectivity, like the function of enzymes in biological systems. For these reasons, these materials represent a promising class of artificial enzymes identified as "nanozymes" due to their nanoscale dimensions. Nanozymes demonstrate exceptional catalytic activity, remarkable chemical and thermal stability, straightforward preparation methods, and the ability to be stored for extended periods without significant degradation.[17,18] Due to their numerous advantages, nanozymes have been regarded as highly promising alternatives to natural enzymes in various applications such as sensors, imaging, disease diagnosis, and therapy.[19,20] Molybdenum disulfide (MoS_2) is a two-dimensional layered nanomaterial with a graphene-like structure that has garnered significant attention due to its distinctive properties and structure.[21] Recent studies have revealed that MoS_2 nanosheets exhibit peroxidase-like activity, making them promising candidates for the development of electrochemical sensors for chemical and biological molecule detection.[22–26] A highly effective approach to enhancing the MoS_2 enzyme-like activity is using MoS_2-based nanocomposites by integrating functional groups into MoS_2 nanosheets. This hybridization strategy has demonstrated significant potential in boosting the enzyme-like performance of MoS_2-based materials. For example, Zribi *et al.* prepared a novel hybrid composite based on a carbon cloth (CC) matrix that was functionalized with 2D-MoS_2 nanosheets and MoO_3. The incorporation of these materials into the CC matrix resulted in improved sensing abilities for riboflavin detection.[27] The compelling findings mentioned above have served as inspiration for the synthesis of MoS_2-based nanocomposites, which proves to be an efficient approach for developing nanozymes exhibiting exceptional enzyme-mimicking activity.

Chitosan (Cs) is a cationic linear polysaccharide with a random distribution of β-(1–4)-linked D-glucosamine and *N*-acetyl-D-glucosamine units,[28] and is both biocompatible and biodegradable. Chitosan–MoS_2 heterojunctions have gained considerable attention for their potential applications in electrochemical sensors. The combination of chitosan with MoS_2 offers unique properties that can enhance the performance of electrochemical sensors.[28] The presence of MoS_2 in the nanocomposite can provide a large surface area, high electrical conductivity, and excellent electrocatalytic activity, making it suitable for the detection of various analytes, including dopamine, while the chitosan matrix acts as a stabilizing agent, providing biocompatibility and enhancing the adhesion of the nanocomposite onto the electrode surface.[29,30] Chitosan–MoS_2 nanocomposites offer several advantages for electrochemical

sensors, such as improved sensitivity, selectivity, and stability. The presence of chitosan can also enhance the biocompatibility of the sensor, making it suitable for biomedical applications.[31]

Herein, this study introduces a novel electrochemical sensor based on chitosan–MoS_2 (Cs–MoS_2) nanocomposites for the sensitive and selective detection of dopamine. This is the first report on the use of Cs–MoS_2 nanocomposites for DA sensing. The Cs–MoS_2 nanocomposite not only enhances the electrocatalytic activity but also provides a biocompatible matrix that improves the adhesion of the material onto the electrode surface. The primary goal of this work is to address the challenges of selectivity and sensitivity in dopamine detection, leveraging the unique properties of Cs–MoS_2. The novelty of this approach lies in the innovative hybridization of MoS_2 with chitosan, offering an advanced material for biomedical applications. The desired outcome is to establish a simple, cost-effective, and efficient sensor capable of accurate DA quantification, paving the way for its application in clinical diagnostics and neurological research.

2. Experimental section

2.1 Synthesis of 2D-MoS_2 nanosheets

MoS_2 powder and sodium cholate were used to synthesize 2D-MoS_2 *via* liquid phase exfoliation.[21] In this process, MoS_2 powder (5 mg mL^{-1}) was dispersed in a SC watery solution (1.5 mg mL^{-1}). This solution was horn sonicated (Branson 250) for 30 min. To decrease the heating effects of sonication, the sample was kept in an ice bath. The dispersion was allowed to be decanted in a flask overnight. Afterward, 20 mL (typically the half-top part) of the solution was centrifuged for 90 minutes at 1500 rpm. The supernatant, rich in a few layers of MoS_2 nanosheets, was collected and the obtained solution remained stable for months.[21]

2.2 Synthesis of the chitosan–MoS_2 nanocomposite

First, the chitosan solution was prepared by dissolving 20 mg of chitosan in 20 mL of acetic acid (1%) with magnetic stirring until a clear solution was obtained. Then, to prepare the Cs (25, 50, and 75)–MoS_2 nanocomposite, different amounts of the chitosan solution were added to pre-synthesized MoS_2 nanosheets, followed by sonication for 25 minutes.

2.3 Characterization

Ultraviolet-visible spectroscopy was carried out using a Lambda 365 UV-vis spectrophotometer from PerkinElmer within the wavelength range of 200–800 nm under ambient air conditions at room temperature.

The atomic force microscopy (AFM) investigation was performed using a Nanosurf instrument equipped with an Easyscan 2 Controller, operating in tapping mode at room temperature. Tapping mode parameters were configured to employ Tap 190 Al-G cantilevers with a frequency of 190 kHz and a force of 48 N m^{-1}. The designation "Tap 190 Al-G" denotes the specific type of cantilever utilized for tapping mode

imaging, typically comprising a silicon base with an aluminum coating. To investigate the shape of the nanosheets, the dispersions were diluted at a ratio of 1:10 with distilled water and subsequently deposited onto glass substrates. The specimens were subjected to air drying at ambient temperature before conducting the experiments.

FTIR spectra were recorded using a spectrum two FTIR spectrometer (PerkinElmer, Inc.) fitted with a universal ATR sampling module. Measurements were performed at room temperature over a spectral range of 4000–500 cm^{-1}, employing a scanning rate of 2 mm s^{-1} and a resolution of 4.0 cm^{-1}. A total of 20 scans were accumulated, with no prior sample preparation. The TGA analysis was performed using a PerkinElmer TGA4000 thermogravimetric analyzer. The procedure was as follows: isothermal at 50 °C for 1 minute, followed by a temperature scan (ramp from 50 to 100 °C at 20 °C min^{-1}), isothermal at 100 °C for 10 minutes, and then a ramp from 100 to 600 °C at 40 °C min^{-1}. To acquire the Raman spectra, 2D-MoS$_2$ and 2D-MoS$_2$/Cs were drop-cast onto a glass substrate, while chitosan was drop-cast onto a gold substrate to quench the fluorescence effect. Raman spectra of the three samples were acquired using a 532 nm excitation wavelength with a 100× objective, focusing the laser spot on a sub-micron area.

2.4 Sensor preparation and electrochemical measurements

Electrochemical analysis was conducted utilizing commercial screen-printed carbon electrodes (SPCEs) procured from Drop-Sens, Spain (DRP-100). The SPCEs were modified with Cs–MoS$_2$ nanocomposite solutions of varying proportions of chitosan solution (25, 50, and 75%), as well as with pure MoS$_2$ dispersion and pure chitosan solution, achieved through drop-casting of appropriate volumes (10, 20, 40, and 60 μL) onto the working electrode surface. Subsequently, the modified electrode was allowed to dry at room temperature before further use.

Electrochemical tests, including cyclic voltammetry and differential pulse voltammetry, were performed using a Drop-Sens μStat 400 potentiostat, controlled using DropView 8400 software for data acquisition. Electrochemical impedance spectroscopy was conducted utilizing a potentiostat/galvanostat. All experiments were carried out at room temperature.

3. Results and discussion

3.1. Optical and morphological characterization

The optical properties of pure samples and their hybrid nanocomposite were studied using UV-vis spectroscopy. Fig. 1 shows the UV-vis spectra of pure MoS$_2$ nanosheets (a), pure chitosan solution (b), and the Cs–MoS$_2$ hybrid nanocomposite (c), covering the wavelength range from 200 to 900 nm. To minimize the effects of multiple scattering during measurements and enable accurate concentration estimation using Beer's law, samples were diluted at a 1:10 v/v ratio in SC before analysis.[21,32–34] All materials have unique absorption spectra, with modest differences in absorption maxima. MoS$_2$ nanosheets (Fig. 1a) exhibit four transitional peaks denoted as A and B excitonic peaks at 673 nm and 613 nm, respectively, and a C-excitonic band at 400–460 nm,
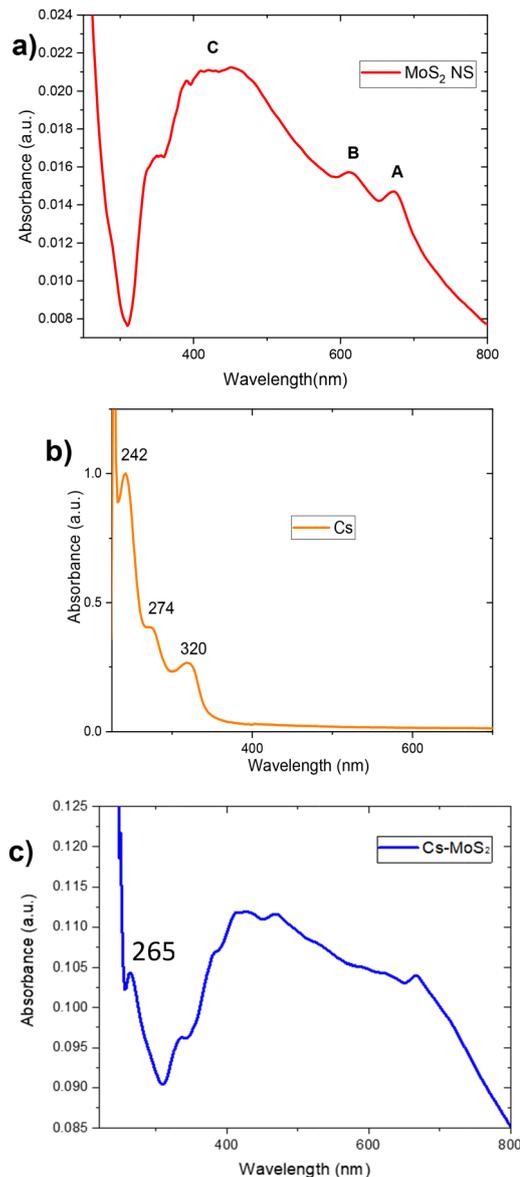

Fig. 1 UV-vis spectra of MoS$_2$ (a), chitosan solution (b), and the Cs–MoS$_2$ hybrid nanocomposite (c).

superposed on a continuum scattering background. The signal is consistent with what was expected for few-layered 2H-MoS$_2$ nanosheets.[21,32,35] Pure chitosan solution (Fig. 1b) has maximal absorption at 274 nm, attributed to the intrinsic bandgap of polysaccharide molecules. This peak corresponds to the n → σ* electronic transitions primarily associated with the chitosan structure's amino and hydroxyl functional groups.[35,36] The absorption peak observed at 320 nm, which is atypical for pure chitosan, can be attributed to residual reagents, trace impurities, or possible structural modifications introduced during the synthesis or processing steps. These modifications may include forming unsaturated or aromatic groups, which could result in additional electronic transitions and contribute to the observed absorption in this region. The UV-visible absorption range of the chitosan–MoS$_2$ hybrid nanocomposite (Fig. 1c) is

260–440 nm, confirming the existence of chitosan–MoS_2 molecules inside the nanocomposite.[35]

The presence of A and B modes, located at 673 nm and 613 nm, respectively, is ascribed to direct excitonic transition at the K-point of the Brillouin zone of MoS_2 nanosheets.[37,38] These modes confirm the spin–orbit splitting of the d-orbital of the molybdenum (Mo) atom. The A–B separation energy is around 0.18 eV, which is inconsistent with the previous studies.[39]

This energy separation ($\Delta E = E_B - E_A$) is dependent on the number of layers. However, only the A-mode position is closely related to this number. In contrast, the B-mode position is unaffected. Thus, it is considered as a thickness indicator.[40,41] According to Backes *et al.*, the wavelength of the A-mode (λ_A) increases when the number of layers per nanosheet increases due to confinement effects.[42] We observed two excitonic bands in the higher energy range, which are denoted as C and D modes located at 452 nm and 3 nm, respectively. This doublet is ascribed to the interlayer coupling by van der Waals forces that involve the p-orbital of S-atoms.[39] According to the research of Castellanos-Gomez, the C-peak position significantly depends on the layer number.[41]

According to the UV-vis spectrum, the size, thickness, and nanosheet concentration in the dispersion can be estimated using empirical metrics mentioned by Backes *et al.*[42,43] and Varrla *et al.*[44] The nanosheet thickness ($\langle N \rangle$) can be estimated based on the wavelength of the A-band (λ_A (nm)):

$$\langle N \rangle = 2.3 \times 10^{36} \exp[-54\,888/\lambda_A] \tag{1}$$

The average nanosheet size ($\langle L \rangle$) was estimated from the ratio between the intensity of the local minimum extinction at 350 nm (Ext 350) and the intensity of the B-exciton (Ext B) using the following equation:

$$\langle L(\text{nm}) \rangle = \frac{3.5 \times \dfrac{\text{Ext}_{max}}{\text{Ext}_{min}} - 0.14}{11.5 - \dfrac{\text{Ext}_{max}}{\text{Ext}_{min}}} \tag{2}$$

Using Beer's law, the nanosheet dispersion concentration C can be determined by considering the extinction coefficient $\varepsilon_{350} = 69$ mL mg^{-1} cm^{-1} at the local minimum (350 nm, [Ext]$_{350}$) and $l = 1$ cm.

$$C = [\text{Ext}]_{350}/l\varepsilon_{350} \tag{3}$$

The sample's characteristics extracted from the UV-vis spectrum of MoS_2 nanosheet dispersion are as follows: $\langle N \rangle = 9$; $\langle L \rangle = 30.3$; and C (μg mL^{-1}) = 2.4.

AFM analysis was conducted to elucidate the morphological properties of the samples. In Fig. 2, we present the AFM images of MoS_2 nanosheets and the Cs–MoS_2 nanocomposite, as well as pure chitosan solution deposited on a glass substrate. A closer examination of the AFM images demonstrates that the integration of chitosan into MoS_2 nanoflakes resulted in a noticeable change in the surface morphology compared to pure MoS_2. Notably, the addition of chitosan led to a rougher surface morphology.

Moreover, the height profile analysis of MoS_2 nanoflakes indicated a thickness of approximately 4.7 nm. Given the
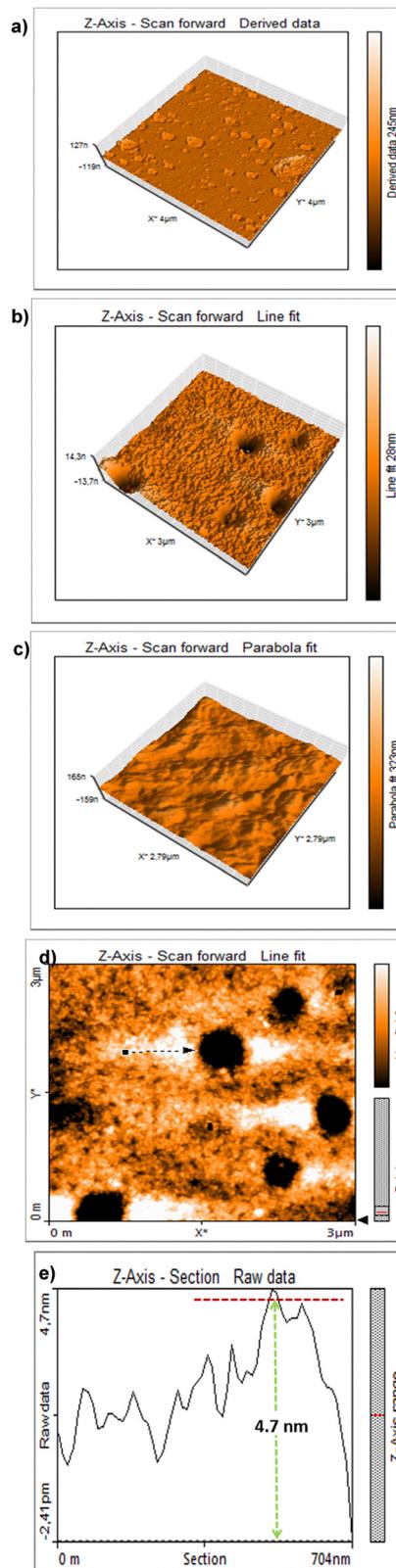

Fig. 2 AFM images of composites deposited on a glass substrate: (a) MoS_2 nanosheets, (b) the Cs–MoS_2 nanocomposite, and (c) chitosan solution, and (d) and (e) the line profile.

theoretical thickness value of monolayer MoS_2 as 0.65 nm, it can be inferred that the exfoliated MoS_2 sample comprises either seven or eight layers. These findings align with the results obtained using UV-visible spectroscopy.

Thermogravimetric analysis (TGA) is an essential tool for characterizing composites, providing critical information on their thermal stability and decomposition behaviour. From the thermal stability analysis of the $Cs-MoS_2$ composite (Fig. 3a), a first weight loss (a) is observed between 50 and 100 °C, likely due to the moisture content, which is confirmed by the FTIR spectrum showing the presence of OH groups. The thermal degradation leads to a second stage of decomposition (b), resulting in a weight loss of about 40% in the 255–350 °C range, attributable to the degradation of chitosan polymer chains. This is followed by a third weight loss at temperatures above 460 °C (c). This behaviour is supported by ref. 35 and 45. The FTIR spectra (Fig. 3b) confirm the successful synthesis of the composites. The characteristic stretching vibrations of MoS_2, typically observed in the range of 450–500 cm^{-1}, exhibit slight variations in intensity, indicating interactions between the MoS_2 nanosheets and the functional groups of chitosan. Specifically, the bands at 613 cm^{-1} and around 900 cm^{-1} correspond to MoS_2 groups.[46,47] The distinctive peaks associated with carbon are located approximately at 1560, 1414 and 1080 cm^{-1}, which correspond to the vibrations of $C=C$, COO^-, and $C-C$ bonds, respectively.[48] The broad band in the range of
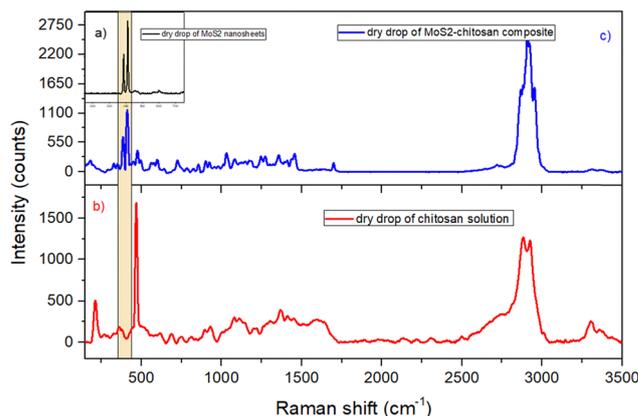
Fig. 4 Raman spectra recorded at 532 nm of dry drops of (a) 2D-MoS_2 nanosheets, (b) chitosan, and (c) the MoS_2/Cs composite.

3000–3600 cm^{-1} is typically associated with O–H stretching vibrations.

The Raman spectra of MoS_2 nanosheets, the chitosan solution, and the MoS_2–chitosan nanocomposite were analysed to elucidate their structural and vibrational properties as shown in Fig. 4. The spectrum of the MoS_2 nanosheets exhibited prominent peaks at $\sim$386 cm^{-1} and $\sim$410 cm^{-1}, corresponding to the in-plane E_{2g}^1 and out-of-plane A_{1g} vibrational modes, respectively.[35,49]

The E_{2g}^1 mode results from the opposite vibration of two S atoms with respect to the Mo atoms in the layers, whereas the A_{1g} mode involves the vibration of only the S atoms out of the layers along the c-axis.[35,49] These modes are typically characteristic of the 2H phase on a few layers of MoS_2.[50] The spectrum of the chitosan solution displayed characteristic peaks at $\sim$1380 cm^{-1} and $\sim$1600 cm^{-1}, attributed to the stretching vibrations of C–N and $C=O$ groups, respectively.[51] In the MoS_2–chitosan composite, both MoS_2 and chitosan peaks are present, with noticeable shifts and broadening. The shifts in the E_{2g}^1 and A_{1g} modes of MoS_2, coupled with modifications in the chitosan peaks, indicate strong interactions between MoS_2 nanosheets and the chitosan matrix, likely mediated by hydrogen bonding and electronic coupling.[35,52] These observations confirm the successful functionalization of chitosan on the MoS_2 nanosheet surfaces and suggest modifications to the vibrational and electronic properties of the composite, which may enhance its functional performance.[35,52]

3.2 Electrochemical behaviour of Cs–MoS_2/SPCE

Cyclic voltammetry (CV) and electrochemical impedance spectroscopy (EIS) measurements were first carried out to examine the significant characteristics of the modified electrodes, such as electrical conductivity and electrocatalytic features. Both experiments were carried out in 0.1 M KCl containing 5 mM of the $[Fe(CN)_6]^{3-/4-}$ redox probe at room temperature. Fig. 5 compares the CV curves of the bare SPCE (black line) and modified SPCEs (coloured lines) in 5 mM of $[Fe(CN)_6]^{3-/4-}$ at a 50 mV s^{-1} scan rate. A pair of well-defined redox peaks were observed in the bare SPCE due to the characteristic reversible redox behaviour of the $[Fe(CN)_6]^{3-/4-}$ system. The anodic peak current of the modified electrodes decreases at first with a low concentration of Cs going
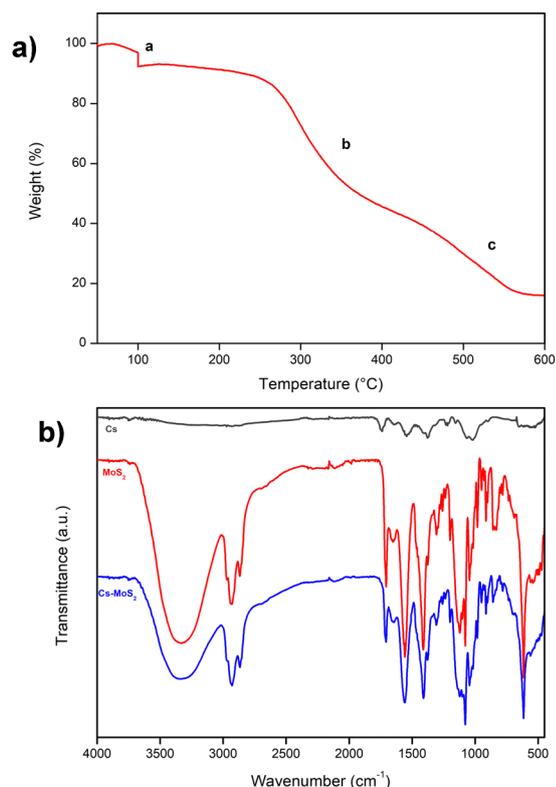

Fig. 3 (a) Thermal stability of the Cs–MoS_2 composite and (b) FTIR spectra of Cs (black line), MoS_2 (red line) and the Cs–MoS_2 composite (blue line).
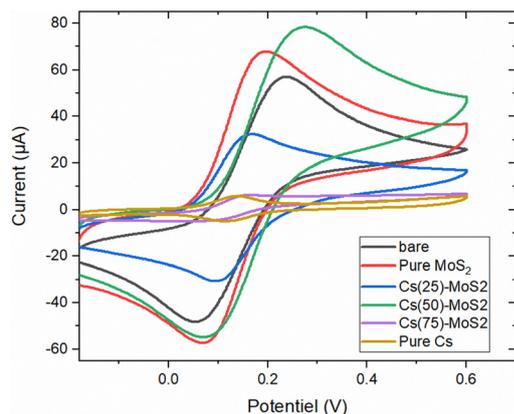
Fig. 5 CV curves of the bare SPCE (black) and the SPCEs (colored lines) modified with different Cs–MoS$_2$ dispersion ratios. Measurements were performed in 0.1 M KCL solution containing 5 mM of [Fe (CN)$_6$]$^{3-/4-}$.

Fig. 6 Calculated electrochemical active surface areas of the different electrodes.

from 57.24 μA for the bare electrode to 32.32 μA for 25% of Cs, suggesting that low Cs hampered the charge transfer at the interface. Reaching 50% of Cs in solution, the anodic peak current undergoes a dramatic increase from 32.32 μA to 78.25 μA. Beyond this optimum ratio between 2D-MoS$_2$ and Cs, a decrease of the peak current is noted. This finding suggests that SPCEs with 50% of Cs provide the best electroanalytic sensitivity among all the presented modified electrodes. We also observed some shifts in the redox peak potentials of the model ferro/ferricyanide redox couple, particularly the anodic peak, at electrodes decorated with various Cs–MoS$_2$ ratios. However, apart from the sample Cs(50)–MoS$_2$, which displays a larger increase in the anodic peak potential with respect to the bare and pure MoS$_2$ ones, the other samples show a modest decrease. This unclear trend is hard to explain, and further investigation is needed in to formulate a plausible explanation.

The Randles–Sevcik equation was used to determine the electroactive surface area of bare and modified electrodes.[53]

$$I_{pa} = 2.686 \times 10^5 n^{3/2} ACD^{1/2} \vartheta^{1/2} \qquad (4)$$

where I_{pa} is the current (in Ampere), n is the number of electrons involved in the redox process ($n = 1$ in our case), A is the effective area of the SPCE (in cm^2), C is the concentration of electroactive species (5×10^{-3} mol cm^{-3}), D is the diffusion coefficient of potassium ferricyanide (7.6×10^{-6} cm^2 s^{-1}), and ϑ is the scan rate (in V s^{-1}). Fig. 6 shows the electroactive surface area (ESA) of bare and modified SPCEs computed using eqn (4). An increase in the active surface area yields an increase in the number of active sites suitable for electrochemical reactions. Consequently, more molecules undergo redox reactions at the surface of modified SPCEs. Data suggested that at a Cs–MoS$_2$ ratio with 50% Cs the ESA is maximized. At higher ratios, the presence of Cs will act as a blocking layer and minimize the electrochemically active sites.

CV tests were performed at different scan rates ranging from 10 mV s^{-1} to 300 mV s^{-1} (Fig. 7a). Fig. 7b shows the anodic (black) and cathodic (red) peak currents plotted against the square root of the scan rate. As expected, a linear behaviour is
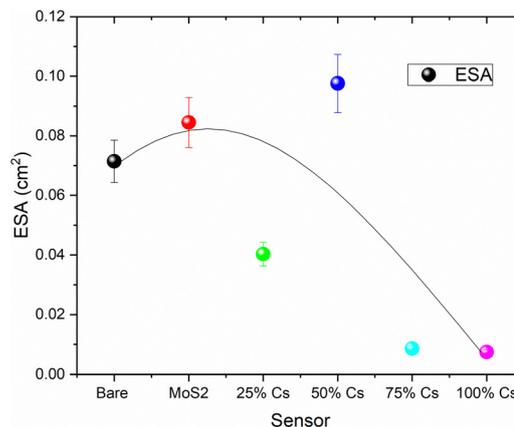
observed, with correlation coefficients (R^2) of 0.9987 and 0.9904, respectively, proving that the diffusion-controlled electron process is dominant at the ferrocyanide and Cs–MoS$_2$/SPC interface.

The Nyquist plots are commonly used in electrochemistry to analyse the impedance of electrochemical systems. They graphically represent the imaginary component (Z'') of impedance
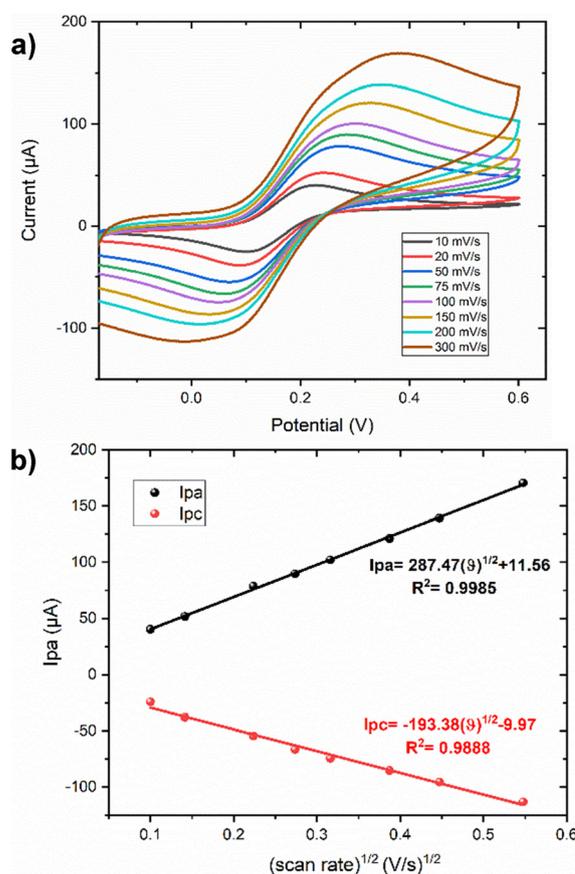

Fig. 7 (a) CV recorded at different scan rates on Cs–MoS$_2$–SPCEs in 0.1 M KCl containing 5 mM of [Fe(CN)$_6$]$^{3-/4-}$; (b) plots of the anodic (black) and cathodic (red) peak currents vs. the square root of the scan rate.

against the real component (Z') on a Cartesian coordinate system.[54,55] Typically, the Nyquist plots exhibit a semi-circular arc followed by a linear tail at high frequencies. The semicircle corresponds to the charge transfer resistance (R_{ct}) at the electrode–electrolyte interface, with larger semicircles indicating higher R_{ct} values.[54,55] Superior electrodes are characterized by smaller semi-circular arcs and extended linear tails, suggesting faster electron transfer kinetics and improved electrochemical performance.[54]

Conversely, poorer electrodes display larger semi-circular arcs and shorter linear tails, indicating slower charge transfer kinetics and inferior behaviour. Analysis of the Nyquist plots commonly involves the Randles equivalent circuit, comprising solution resistance (R_S) in series with a parallel combination of double-layer capacitance (C_{dl}) and Warburg impedance.[54,55] Fitting experimental data to this circuit allows the determination of various electrochemical parameters critical for assessing sensor performance.[54,55] The charge transfer resistance (R_{ct}) is a key parameter directly linked to redox reaction kinetics: larger R_{ct} values imply slower kinetics, while smaller values indicate faster kinetics.[54]

Fig. 8a shows the Nyquist plots of the EIS conducted on the bare SPCE, Cs(25)–MoS$_2$–SPCE, Cs(50)–MoS$_2$–SPCE, Cs(75)–MoS$_2$–SPCE, as well as pure MoS$_2$ and chitosan modified SPCEs, which were obtained in 5 mM [Fe(CN)$_6$]$^{3-/4-}$ solution containing 0.1 M KCl. Notably, the arc diameter of the Cs(50)–MoS$_2$–SPCE appeared to be the smallest, indicative of reduced resistance to charge transport compared to bare and other modified SPCEs. However, the arc diameter proportionally increased as the Cs content increased in the hybrid nanocomposite. The observed semicircular pattern in the high-frequency region corresponds to the charge transfer resistance at the electrode–electrolyte interface.[56] A smaller diameter of the semi-circular arc suggests lower charge transfer resistance and relatively higher capacitance.[56]

In this study, the obtained results were fitted into the model of an RC circuit, as illustrated in Fig. 8b, wherein R_{ct} represents
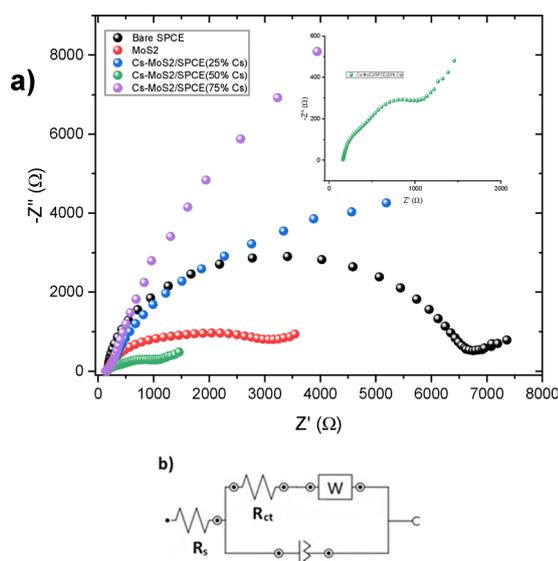
Table 1 Charge transfer resistance of the different electrodes

Electrode	R_{ct} (kΩ)
Bare SPCE	14.9
Pure MoS$_2$	2.4
Cs(25)–MoS$_2$	11.8
Cs(50)–MoS$_2$	1.8
Cs(75)–MoS$_2$	49.5
Pure Cs	120

the interfacial charge-transfer resistance of the photoanode/electrolyte interface. As presented in Table 1, a reduced charge transfer resistance was observed for the Cs(50)–MoS$_2$/SPCE compared to the Cs(25)–MoS$_2$/SPCE, Cs(75)–MoS$_2$/SPCE, and the bare SPCE. This result indicates the enhanced electron transport nature of the Cs(50)–MoS$_2$/SPCE, attributed to the integration of 50% Cs in the composite, facilitating easier and more rapid electron exchange between the electrode surface and electrolyte interface.[57]

This finding implies that the nanocomposite-modified electrode exhibits faster electron transfer behaviour, possibly attributed to the positive charge of the electrode–electrolyte interface, which is associated with a higher degree of amidation.[31] In this instance, the degree of amidation refers to the extent of amide group incorporation within the chitosan structure. Amidation involves transforming some carboxyl groups in chitosan into amide groups, potentially leading to a higher positive charge at the electrode–electrolyte interface. This increased positive charge can enhance the electrochemical properties of the electrode, facilitate faster electron transfer kinetics, and ultimately improve the performance of the chitosan–MoS$_2$-modified electrode in electrochemical reactions.[31]

In this study, we observed that varying the chitosan content in the chitosan–MoS$_2$ hybrid nanocomposite significantly impacts its electroactive surface area (ESA) and charge transfer resistance (R_{ct}). Pure MoS$_2$ exhibited high ESA due to its large surface area, but its lack of stability without a binder was a limiting factor. Conversely, pure chitosan, being insulating, demonstrated low ESA and high R_{ct}. Incorporating 25% chitosan into the composite decreased ESA, likely due to insufficient chitosan to prevent MoS$_2$ aggregation, leading to a reduced active surface area. However, the composite with 50% chitosan displayed the highest ESA and the lowest R_{ct}, indicating an optimal balance where chitosan provided sufficient mechanical support and dispersion of MoS$_2$ without excessively blocking its active sites. In contrast, a 75% chitosan content led to significant encapsulation of MoS$_2$, reducing ESA and increasing R_{ct} due to the insulating nature of the polymer. These findings indicate that the composite's electrochemical performance depends on achieving an optimal chitosan-to-MoS$_2$ ratio, with 50% chitosan offering the best synergy between stability and electroactivity.

3.3 Optimization of experimental conditions

Preliminary tests for investigating the performances of the bare and modified electrodes were carried out by cyclic voltammetry in 0.01 M PBS (pH 7.4) containing 100 µM of DA at a 50 mV s^{-1}

Fig. 8 (a) The Nyquist plots and (b) simulated equivalent circuit of bare and modified SPCEs.

scan rate (Fig. 9). At the Cs(50)–MoS$_2$–SPCE, anodic peak currents (I_{pa}) occur at more negative potentials compared to the bare SPCE, while cathodic peak currents (I_{pc}) are observed at more positive potentials. Specifically, the anodic peak current at the Cs(50)–MoS$_2$–SPCE was 13.06 μA, compared to 3.42 μA at the bare SPCE, indicating improved conductivity due to the hybrid composite. The observed negative shift in anodic peak potentials (E_{pa}) indicates improved electrochemical performance of the Cs(50)–MoS$_2$–SPCE, attributed to enhanced electron transfer kinetics and increased electroactive surface area.[58,59] Conversely, the bare SPCE is more susceptible to fouling, resulting in compromised electron transfer kinetics over time.[58,60] The peak-to-peak separation of the anodic and cathodic peak potentials (ΔE_p) is considered an index of the redox reaction reversibility and electron transfer kinetics.[58] The obtained ΔE_p values (97 mV for the bare SPCE and 47 mV for the Cs(50)–MoS$_2$–SPCE) confirm that the modified electrode supports more reversible DA redox processes, faster electron transfer kinetics, and better catalytic activity. The Cs–MoS$_2$ composite may facilitate π–π interactions between DA and the aromatic moieties in chitosan, along with potential electrostatic interactions due to oxygen-containing functionalities, enhancing conductivity and sensitivity in DA detection.

The effect of Cs(50)–MoS$_2$ hybrid nanocomposite loading, deposited on SPCEs, was investigated concerning its sensing behaviour towards dopamine using the DPV test. Carbon SPCEs were modified by adding various volumes of the as-prepared hybrid nanocomposite dispersion, ranging from 10 to 60 μL. The results of the electrochemical investigation with Cs–MoS$_2$/SPCE are presented in Fig. 10. In the range of 10 μL to 60 μL, the sensitivity increased with the increasing modified volume of Cs–MoS$_2$ suspension deposited onto the SPCE surface. The further increase in the modified volume will cause a gradual decrease in the sensitivity of our sensors. Therefore, the electrode containing 10 μL of Cs(50)–MoS$_2$ suspension was selected as the best electrode to carry out the subsequent experiments.

The effect of the scan rate on the redox peak currents of DA oxidation at the Cs–MoS$_2$ modified SPCE surface was studied
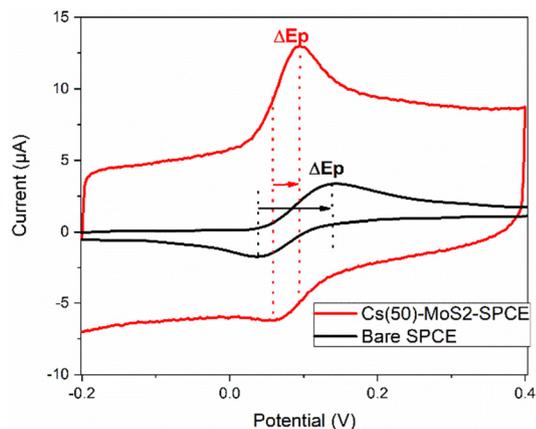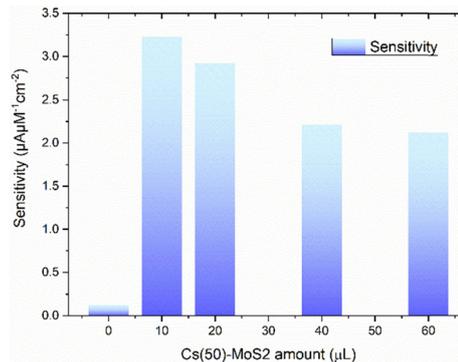

Fig. 10 The effect of different amounts of the active electrode material (Cs(50)–MoS$_2$) on sensitivity towards the detection of dopamine using the DPV test.

using cyclic voltammetry. Cyclic voltammograms were recorded with Cs(50)–MoS$_2$/SPCE (10 μL) at scan rates from 20 to 200 mV s^{-1} in 0.01 M phosphate buffer saline (PBS) containing 100 μM DA as shown in Fig. 11a. The DA redox peak current increased with the square root of the scan rate and a linear correlation was observed. In addition, as the scan rate increases, there is a discernible shift of the oxidation and reduction peak potentials towards the positive and negative regions, respectively. This occurrence is indicative of a reduced rate of electron transfer at faster scan rates. At the same time, the ΔE_p values increased, suggesting that, at higher scan rates, the electron transfer process becomes quasi-reversible. Fig. 11b

Fig. 9 CV of 100 μM DA recorded on the bare SPCE and Cs(50%)–MoS$_2$–SPCE in 0.01 M PBS (pH 7.4) at a 50 mV s^{-1} scan rate.
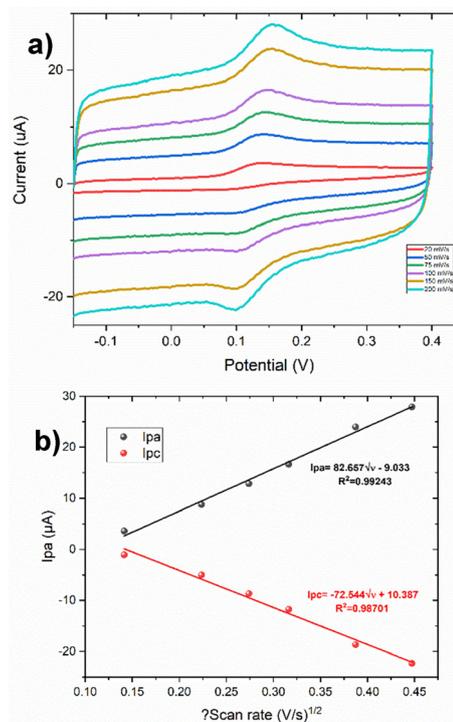

Fig. 11 (a) Cyclic voltammograms in the presence of 100 μM DA at different scan rates with Cs–MoS$_2$ (50% Cs, 10 μL) SPCE. (b) The plots of peak currents *vs.* the square root of the scan rate.

presents the regression equations that can be expressed as follows: $I_{pa} = 82.66(v)^{1/2} - 9.03$ ($R^2 = 0.992$), $I_{pc} = -72.54(v)^{1/2} + 10.39$ ($R^2 = 0.987$), which confirms that the electrochemical process at the modified electrode surface is controlled by diffusion.[61]

The electrochemical performance of the bare SPCE, MoS_2–SPCE, and Cs–MoS_2–SPCE for dopamine detection was investigated also by DPV. This technique exhibits higher sensitivity and a lower limit of detection compared to the CV technique for quantitative analysis, applying a small voltage pulse superimposed on the linear voltage sweep and sampling the differential current shortly after the pulse.[31,62] Consequently, DPV was utilized to evaluate the performance of the Cs–MoS_2 matrix for the quantitative determination of dopamine in 0.01 M PBS containing 100 μM DA as shown in Fig. 12.

On the bare SPCE surface, a small peak corresponding to DA oxidation was observed. However, upon modification of the SPCE with MoS_2, a significant enhancement of the DPV response was achieved. Notably, the Cs–MoS_2–SPCE exhibited the highest response compared to both the bare SPCE and the MoS_2–SPCE in terms of dopamine oxidation. This result demonstrates the superior electrochemical performance of the Cs–MoS_2 modified electrode, suggesting the effective synergistic interaction between chitosan and MoS_2 in enhancing the catalytic activity and sensitivity towards dopamine oxidation by providing a higher surface area and more active sites and also facilitating the electron transfer between the analyte and the electrode.

Calibration curves derived from the DPV test were used to compare the bare SPCE and Cs–MoS_2–SPCEs (0%, 25%, 50%, and 75% chitosan) in various DA concentrations ranging from 0 to 100 μM (Fig. 13a). The sensitivity (extracted from the slope of calibration curves) towards dopamine increased sharply with the increase in the amount of chitosan, up to 50% (Fig. 13b). This behaviour can be attributed to the presence of chitosan. Increasing the amount of chitosan in the nanocomposite provides more active sites and functional groups for analyte adsorption. Improved electrochemical performance leads to enhanced signal generation and improved sensitivity in electrochemical sensors. However, since chitosan is an insulating
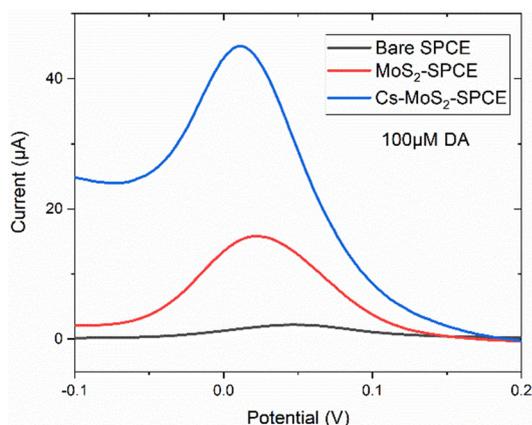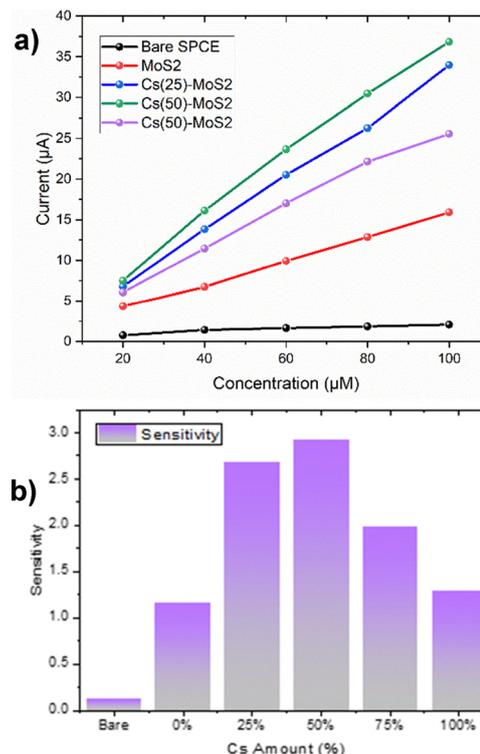

Fig. 13 (a) Calibration curves from the DPV technique of bare and modified SPCEs with different amounts of chitosan. (b) The effect of different amounts of chitosan on sensitivity.

polymer, at high content, it can slow down mass transport and sensitivity. Excessive chitosan content can also reduce the effective active surface area available for analyte adsorption and interaction, limiting the contact between the analyte and the electrode surface. In addition, chitosan contain functional groups that can interact with different compounds. This could lead to non-specific adsorption or interference from other parts of the sample. Higher chitosan amounts may increase the likelihood of non-specific interactions, compromising the sensor's selectivity and sensitivity for the target analyte. Thus, the nanocomposite synthesized with 50% of Cs content was selected for further investigations.

3.4 Quantitative determination of dopamine

The DPV responses of the optimized sensor in various DA concentrations in 0.01 M PBS are depicted in Fig. 14a. The peak current corresponding to DA oxidation increases with increasing DA concentration from 0 to 440 μM. These findings validate the successful performance of our sensor in detecting a wide range of DA concentrations. The observed increase in the peak current in the lower and higher DA concentration ranges confirms the reliable detection and quantification of DA using the DPV method. These results provide valuable insights into the dynamic range and sensitivity of the sensor for DA analysis.

The calibration curve shows the presence of two distinct linear operating ranges (Fig. 14b). The first linearity range is from 0 to 40 μM (red line, $R^2 = 0.991$) where the sensor exhibits a sensitivity of 4.48 μA μM^{-1} cm^{-2}. The second linear range is

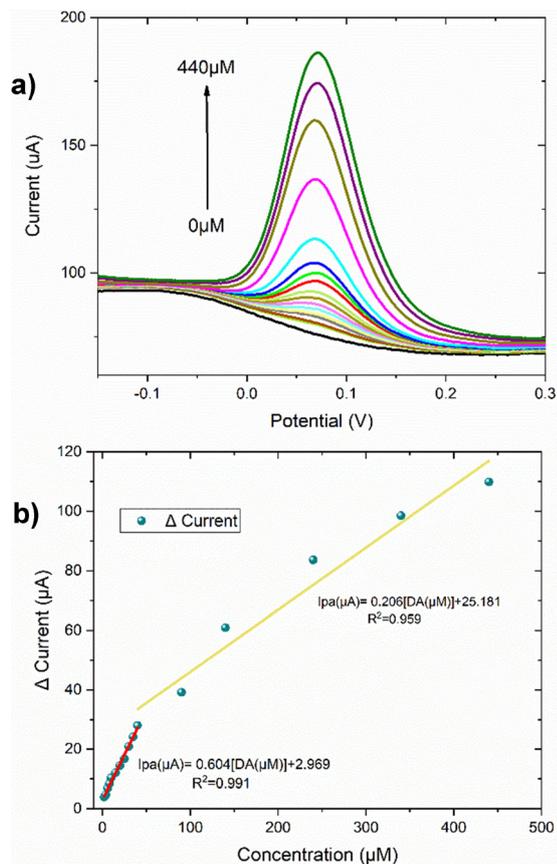Fig. 12 DPV response on 100 μM DA recorded on bare, MoS_2, and Cs–MoS_2 modified SPCEs in 0.01 M PBS.

Fig. 14 (a) DPV curves on Cs−MoS$_2$−SPCE at various concentrations of DA (0−440 μM) in 0.01 PBS. (b) Calibration curves of Cs−MoS$_2$−SPCE towards dopamine concentration.

from 40 to 440 μM (yellow line, R^2 = 0.959) and the calculated sensitivity is 1.67 μA μM^{-1} cm^{-2}. The limit of detection (LOD) of this sensor is 0.8 μM. Overall, the electrode devised in this study exhibits suitability for use as a dopamine sensor.

The sensitivity, LOD and linear dynamic range (LDR) of the proposed Cs−MoS$_2$−SPCE based sensor were compared with the most recently reported dopamine electrochemical sensors as presented in Table 2. Our Cs−MoS$_2$−SPCE sensor is shown to have remarkable performance characteristics, with the best sensitivity in the lower concentration regime.

3.5 Effect of potentially interfering species

A crucial aspect determining the applicability of a biosensor is its capacity to selectively differentiate analytes from interferents. In this study, the electrochemical responses of 100 μM DA on Cs−MoS$_2$ in the presence of various interferents was studied. The impact of various bioorganic species, including L-tyrosine, uric acid, urea, ascorbic acid, and glucose, as well as common inorganic ions such as Na$^+$ and K$^+$, on the electrochemical response of dopamine was investigated. The results are shown in Fig. 15, revealing that there were no significant changes in the current response of dopamine in the presence of L-tyrosine, uric acid, glucose, urea, ascorbic acid, sodium ions, and potassium ions.

These findings indicate that the sensor exhibits excellent selectivity for the determination of dopamine (DA) even in the presence of various interfering bioorganic and/or inorganic ions.

3.6 Reproducibility and repeatability

The reliability of the developed sensor was evaluated through assessments of the signal reproducibility and fabrication repeatability. The reproducibility of the sensor was examined by conducting four consecutive measurements of the peak current for DA oxidation using the same electrode (Fig. 16a). Meanwhile, the relative standard deviation (RSD, n = 4) was calculated and found to be 0.06. Additionally, two distinct Cs−MoS$_2$ electrodes were prepared to investigate the repeatability of the sensor's fabrication methodology (Fig. 14b). The relative standard deviation (RSD n = 2) was computed to be 0.02. These observations collectively demonstrate the satisfactory reproducibility and repeatability of the prepared electrode.

3.7 Real sample analysis

The practical application of the fabricated sensor was assessed within biological matrices, specifically human serum and saliva samples. Blood serum and saliva specimens were obtained from healthy volunteers and subsequently subjected to centrifugation at 3000 rpm for 10 minutes. Following centrifugation, 1 mL of each sample was diluted 100-fold with 0.01 M phosphate-buffered saline (PBS) at pH 7 as a strategy to reduce nonspecific interferences,[67] and a known concentration of dopamine was introduced as a spike using the standard DA addition method.[68] The detection of dopamine in the spiked real samples was conducted using the differential pulse voltammetry (DPV) technique. The recovered concentration of DA in the spiked samples was 97.49% for blood serum and 105.76% for saliva of the one added, indicating that the detection of dopamine using this procedure is almost free from interferences present in the biological sample matrices.

Table 2 Sensing performance comparison with published works regarding Cs−MoS$_2$-based dopamine electrochemical sensing

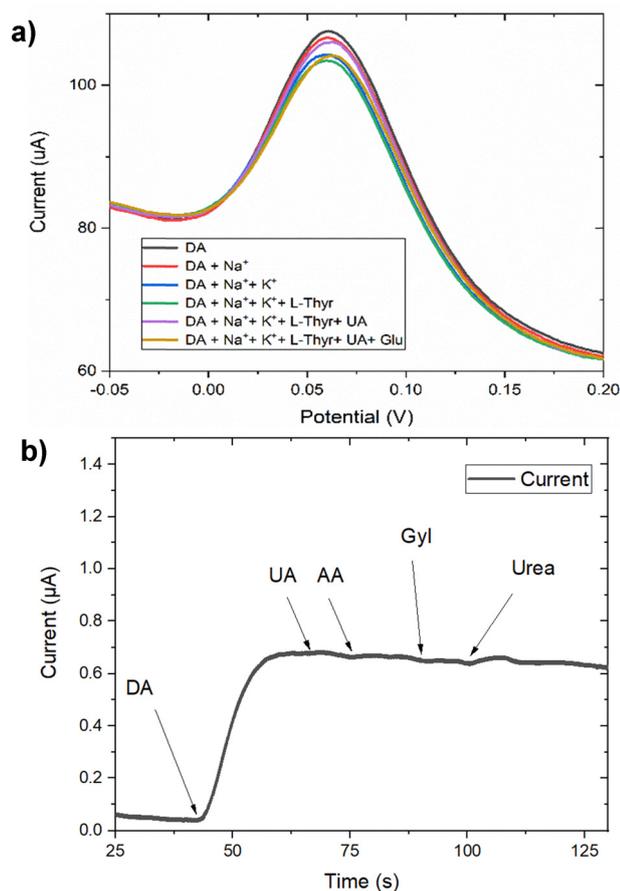| Materials	Linear range (μM)	Sensitivity (μA μM^{-1} cm^{-2})	LOD (μM)	Technique	Ref.
Au/rGO	6.8–41	—	1.4	DPV	63
MoS$_2$	250–4000	0.77	0.3	CV	8
CAuNE	1–100	—	5.83	CV	64
MoS$_2$	1–100	1.044	0.085	DPV	65
Au nanospikes	0.2–50	0.056	0.33	AMP	66
Cs−MoS$_2$	0–40	4.482	0.8	DPV	This work
	40–440	1.672			

Fig. 15 (a) Interference test of the fabricated sensors in the detection of 100 μM DA in 0.01 M PBS using the differential pulse voltammetry technique; (b) interference test of the fabricated sensors in the detection of 100 μM DA in 0.01 M PBS using the chronoamperometry technique.

Fig. 16 (a) Reproducibility test using two different electrodes tested at the same conditions, (b) repeatability test of the same sensor at a fixed concentration.

The resulting findings and recoveries are tabulated in Table 3. Ultimately, the Cs–MoS$_2$–SPCE demonstrated promising efficacy for real-time applications. These results suggested that electrochemical sensors based on Cs–MoS$_2$–SPCEs, as illustrated, could be applied to the determination of dopamine in real samples.

Table 3 Analyses of real biological samples with a Cs–MoS$_2$–SPCE sensor

Sample	Concentration added (μM)	Concentration found (μM)	Recovery (%)	RSD (n = 5)
Blood serum	4	3.89	97.49	0.06
Saliva	4	4.23	105.76	0.44

4. Conclusions

In conclusion, we have modified commercial SPCEs through the deposition of Cs–MoS$_2$ hybrid materials onto the working electrode surface and tested their sensitivity for the electrochemical sensing of DA. The fabrication process of this sensor ensures reliable and efficient production. Through the electroanalytical experiments, it was observed that the Cs–MoS$_2$ modified electrode outperformed both the bare electrode- and MoS$_2$-based sensors in the determination of dopamine (DA) with good sensitivity and LOD values of 4.482 μA μM^{-1} cm^{-2} and 0.8 μM, respectively. Overall, this study successfully demonstrated the utility of the proposed hybrid material as a modifier for fabricating enzyme-free electrochemical sensors for th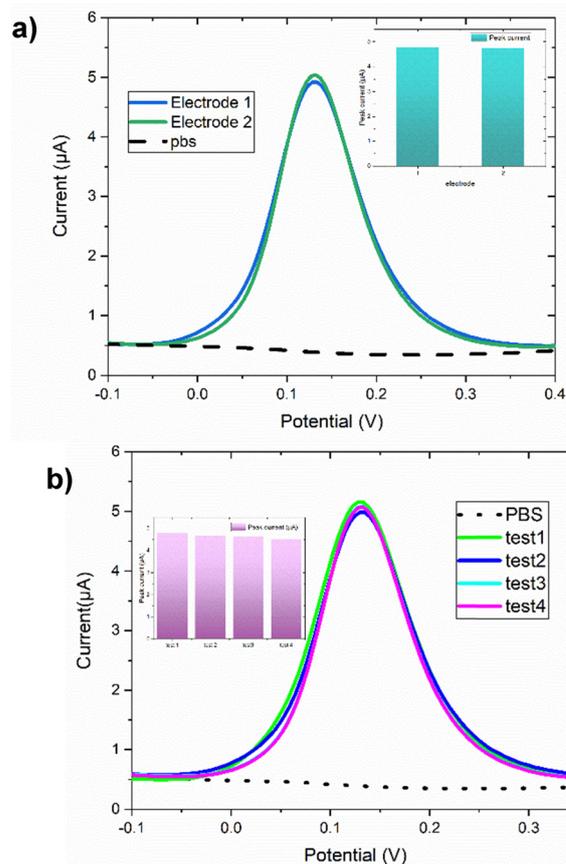e qualitative and quantitative determination of dopamine even in the presence of other interferent species. Such sensors hold significant potential for electroanalytical applications, particularly in the monitoring of biochemical substances.

Author contributions

The manuscript was written through contributions of all authors. All authors have given approval to the final version of the manuscript.

Conflicts of interest

There are no conflicts to declare.

Data availability

All data generated and/or analyzed during this study are available in the main text.

Acknowledgements

References

1 H. Devnani, S. Ansari, S. P. Satsangee and R. Jain, ZrO₂-Graphene-Chitosan Nanocomposite Modified Carbon Paste Sensor for Sensitive and Selective Determination of Dopamine, *Mater. Today Chem.*, 2017, **4**, 17–25, DOI: **10.1016/j.mtchem.2017.02.004**.

2 S. K. Panigrahy, A. Nandha, M. Chaturvedi and P. K. Mishra, Novel Nanocomposites with Advanced Materials and Their Role in Waste Water Treatment, *Sustain*, 2024, **4**, 100042, DOI: **10.1016/j.nxsust.2024.100042**.

3 R. M. Wightman, L. J. May and A. C. Michael, Detection of Dopamine Dynamics in the Brain, *Anal. Chem.*, 1988, **60**(13), 769A–779A, DOI: **10.1021/ac00164a001**.

4 M. L. A. V. Heien, A. S. Khan, J. L. Ariansen, J. F. Cheer, P. E. M. Phillips, K. M. Wassum and R. M. Wightman, Real-Time Measurement of Dopamine Fluctuations after Cocaine in the Brain of Behaving Rats, *Proc. Natl. Acad. Sci. U. S. A.*, 2005, **102**(29), 10023–10028, DOI: **10.1073/pnas.0504657102**.

5 F. Mora, G. Segovia, A. del Arco, M. de Blas and P. Garrido, Stress, Neurotransmitters, Corticosterone and Body–Brain Integration, *Brain Res.*, 2012, **1476**, 71–85, DOI: **10.1016/j.brainres.2011.12.049**.

6 J. W. Dalley and J. P. Roiser, Dopamine, Serotonin and Impulsivity, *Neuroscience*, 2012, **215**, 42–58, DOI: **10.1016/j.neuroscience.2012.03.065**.

7 H. Y. Yue, P. F. Wu, S. Huang, X. Gao, S. S. Song, W. Q. Wang, H. J. Zhang and X. R. Guo, Electrochemical Determination of Dopamine in the Presence of Uric Acid Using WS₂ Nanospheres-Carbon Nanofibers, *J. Electroanal. Chem.*, 2019, **833**, 427–432, DOI: **10.1016/j.jelechem.2018.12.016**.

8 M. Sabar, U. Amara, S. Riaz, A. Hayat, M. Nasir and M. H. Nawaz, Fabrication of MoS₂ Enwrapped Carbon Cloth as Electrochemical Probe for Non-Enzymatic Detection of Dopamine, *Mater. Lett.*, 2022, **308**, 131233, DOI: **10.1016/j.matlet.2021.131233**.

9 R. P. Shukla, M. Aroosh, A. Matzafi and H. Ben-Yoav, Partially Functional Electrode Modifications for Rapid Detection of Dopamine in Urine, *Adv. Funct. Mater.*, 2021, **31**(17), 2004146, DOI: **10.1002/adfm.202004146**.

10 L. Wang, R. Yang, L. Qu, P. Harrington and B. de, Electrostatic Repulsion Strategy for High-Sensitive and Selective Determination of Dopamine in the Presence of Uric Acid and Ascorbic Acid, *Talanta*, 2020, **210**, 120626, DOI: **10.1016/j.talanta.2019.120626**.

11 D. S. Sipuka, O. A. Arotiba, T. I. Sebokolodi, T. R. Tsekeli and D. Nkosi, Gold-Dendrimer Nanocomposite Based Electrochemical Sensor for Dopamine, *Electroanalysis*, 2023, **35**(3), e202200099, DOI: **10.1002/elan.202200099**.

12 M. H. Raza, K. Movlaee, Y. Wu, S. M. El-Refaei, M. Karg, S. G. Leonardi, G. Neri and N. Pinna, Tuning the NiO Thin Film Morphology on Carbon Nanotubes by Atomic Layer Deposition for Enzyme-Free Glucose Sensing, *ChemElectroChem*, 2019, **6**(2), 383–392, DOI: **10.1002/celc.201801420**.

13 Z. Hsine, R. Mlika, N. Jaffrezic-Renault and H. Korri-Youssoufi, Review—Recent Progress in Graphene Based Modified Electrodes for Electrochemical Detection of Dopamine, *Chemosensors*, 2022, **10**(7), 249, DOI: **10.3390/chemosensors10070249**.

14 S. A. Hira, S. Nagappan, D. Annas, Y. A. Kumar and K. H. Park, NO₂-Functionalized Metal–Organic Framework Incorporating Bimetallic Alloy Nanoparticles as a Sensor for Efficient Electrochemical Detection of Dopamine, *Electrochem. Commun.*, 2021, **125**, 107012, DOI: **10.1016/j.elecom.2021.107012**.

15 S. Cai and R. Yang, Two-Dimensional Nanomaterials With Enzyme-Like Properties for Biomedical Applications, *Front. Chem.*, 2020, **8**, 565940, DOI: **10.3389/fchem.2020.565940**.

16 Y. Lyu and P. Scrimin, Mimicking Enzymes: The Quest for Powerful Catalysts from Simple Molecules to Nanozymes, *ACS Catal.*, 2021, **11**(18), 11501–11509, DOI: **10.1021/acscatal.1c01219**.

17 L. Alvarado-Ramírez, M. Rostro-Alanis, J. Rodríguez-Rodríguez, J. E. Sosa-Hernández, E. M. Melchor-Martínez, H. M. N. Iqbal and R. Parra-Saldívar, Enzyme (Single and Multiple) and Nanozyme Biosensors: Recent Developments and Their Novel Applications in the Water-Food-Health Nexus, *Biosensors*, 2021, **11**(11), 410, DOI: **10.3390/bios11110410**.

18 J. Wu, X. Wang, Q. Wang, Z. Lou, S. Li, Y. Zhu, L. Qin and H. Wei, Nanomaterials with Enzyme-like Characteristics (Nanozymes): Next-Generation Artificial Enzymes (II), *Chem. Soc. Rev.*, 2019, **48**(4), 1004–1076, DOI: **10.1039/C8CS00457A**.

19 D. Jiang, D. Ni, Z. T. Rosenkrans, P. Huang, X. Yan and W. Cai, Nanozyme: New Horizons for Responsive Biomedical Applications, *Chem. Soc. Rev.*, 2019, **48**(14), 3683–3704, DOI: **10.1039/C8CS00718G**.

20 X. Wang, Y. Hu and H. Wei, Nanozymes in Bionanotechnology: From Sensing to Therapeutics and Beyond, *Inorg. Chem. Front.*, 2016, **3**(1), 41–60, DOI: **10.1039/C5QI00240K**.

21 R. Zribi, R. Maalej, R. Gillibert, M. G. Donato, P. G. Gucciardi, S. G. Leonardi and G. Neri, Simultaneous and Selective Determination of Dopamine and Tyrosine in the Presence of Uric Acid with 2D-MoS₂ Nanosheets Modified Screen-Printed Carbon Electrodes, *FlatChem*, 2020, **24**, 100187, DOI: **10.1016/j.flatc.2020.100187**.

22 S. Su, Z. Lu, J. Li, Q. Hao, W. Liu, C. Zhu, X. Shen, J. Shi and L. Wang, MoS₂–Au@Pt Nanohybrids as a Sensing Platform for Electrochemical Nonenzymatic Glucose Detection, *New J. Chem.*, 2018, **42**(9), 6750–6755, DOI: **10.1039/C8NJ00940F**.

23 X. Chen, Y. J. Park, M. Kang, S.-K. Kang, J. Koo, S. M. Shinde, J. Shin, S. Jeon, G. Park, Y. Yan, M. R. MacEwan, W. Z. Ray, K.-M. Lee, J. A. Rogers and J.-H. Ahn, CVD-Grown Monolayer

MoS$_2$ in Bioabsorbable Electronics and Biosensors, *Nat. Commun.*, 2018, **9**(1), 1690, DOI: **10.1038/s41467-018-03956-9**.

24 R. Zribi and G. Neri, Mo-Based Layered Nanostructures for the Electrochemical Sensing of Biomolecules, *Sensors*, 2020, **20**(18), 5404, DOI: **10.3390/s20185404**.

25 L. Gong, L. Feng, Y. Zheng, Y. Luo, D. Zhu, J. Chao, S. Su and L. Wang, Molybdenum Disulfide-Based Nanoprobes: Preparation and Sensing Application, *Biosensors*, 2022, **12**(2), 87, DOI: **10.3390/bios12020087**.

26 C. Zhu, Z. Zeng, H. Li, F. Li, C. Fan and H. Zhang, Single-Layer MoS$_2$-Based Nanoprobes for Homogeneous Detection of Biomolecules, *J. Am. Chem. Soc.*, 2013, **135**(16), 5998–6001, DOI: **10.1021/ja4019572**.

27 R. Zribi, A. Foti, M. G. Donato, P. G. Gucciardi and G. Neri, Fabrication of a Novel Electrochemical Sensor Based on Carbon Cloth Matrix Functionalized with MoO$_3$ and 2D-MoS$_2$ Layers for Riboflavin Determination, *Sensors*, 2021, **21**(4), 1371, DOI: **10.3390/s21041371**.

28 K. Kasinathan, B. Murugesan, N. Pandian, S. Mahalingam, B. Selvaraj and K. Marimuthu, Synthesis of Biogenic Chitosan-Functionalized 2D Layered MoS$_2$ Hybrid Nanocomposite and Its Performance in Pharmaceutical Applications: In-Vitro Antibacterial and Anticancer Activity, *Int. J. Biol. Macromol.*, 2020, **149**, 1019–1033, DOI: **10.1016/j.ijbiomac.2020.02.003**.

29 D. Bal Altuntaş and F. Kuralay, MoS$_2$/Chitosan/GO$_x$-Gelatin Modified Graphite Surface: Preparation, Characterization and Its Use for Glucose Determination, *Mater. Sci. Eng., B*, 2021, **270**, 115215, DOI: **10.1016/j.mseb.2021.115215**.

30 A. Prabhu, R. D. Crapnell, K. Eersels, B. van Grinsven, A. K. Kunhiraman, P. Singla, J. McClements, C. E. Banks, K. Novakovic and M. Peeters, Reviewing the Use of Chitosan and Polydopamine for Electrochemical Sensing, *Curr. Opin. Electrochem.*, 2022, **32**, 100885, DOI: **10.1016/j.coelec.2021.100885**.

31 H. Begum, M. S. Ahmed and S. Jeon, New Approach for Porous Chitosan–Graphene Matrix Preparation through Enhanced Amidation for Synergic Detection of Dopamine and Uric Acid, *ACS Omega*, 2017, **2**(6), 3043–3054, DOI: **10.1021/acsomega.7b00331**.

32 R. Zribi, R. Maalej, E. Messina, R. Gillibert, M. G. Donato, O. M. Maragò, P. G. Gucciardi, S. G. Leonardi and G. Neri, Exfoliated 2D-MoS$_2$ Nanosheets on Carbon and Gold Screen Printed Electrodes for Enzyme-Free Electrochemical Sensing of Tyrosine, *Sens. Actuators, B*, 2020, **303**, 127229, DOI: **10.1016/j.snb.2019.127229**.

33 K. R. Paton and J. N. Coleman, Relating the Optical Absorption Coefficient of Nanosheet Dispersions to the Intrinsic Monolayer Absorption, *Carbon*, 2016, **107**, 733–738, DOI: **10.1016/j.carbon.2016.06.043**.

34 A. Quirantes, F. Arroyo and J. Quirantes-Ros, Multiple Light Scattering by Spherical Particle Systems and Its Dependence on Concentration: A T-Matrix Study, *J. Colloid Interface Sci.*, 2001, **240**(1), 78–82, DOI: **10.1006/jcis.2001.7641**.

35 K. Kasinathan, B. Murugesan, N. Pandian, S. Mahalingam, B. Selvaraj and K. Marimuthu, Synthesis of Biogenic

Chitosan-Functionalized 2D Layered MoS$_2$ Hybrid Nanocomposite and Its Performance in Pharmaceutical Applications: In-Vitro Antibacterial and Anticancer Activity, *Int. J. Biol. Macromol.*, 2020, **149**, 1019–1033, DOI: **10.1016/j.ijbiomac.2020.02.003**.

36 N. Islam, H. Wang, F. Maqbool and V. Ferro, In Vitro Enzymatic Digestibility of Glutaraldehyde-Crosslinked Chitosan Nanoparticles in Lysozyme Solution and Their Applicability in Pulmonary Drug Delivery, *Molecules*, 2019, **24**(7), 1271, DOI: **10.3390/molecules24071271**.

37 N. Wang, F. Wei, Y. Qi, H. Li, X. Lu, G. Zhao and Q. Xu, Synthesis of Strongly Fluorescent Molybdenum Disulfide Nanosheets for Cell-Targeted Labeling, *ACS Appl. Mater. Interfaces*, 2014, **6**(22), 19888–19894, DOI: **10.1021/am505305g**.

38 M. Kukkar, A. Sharma, P. Kumar, K.-H. Kim and A. Deep, Application of MoS$_2$ Modified Screen-Printed Electrodes for Highly Sensitive Detection of Bovine Serum Albumin, *Anal. Chim. Acta*, 2016, **939**, 101–107, DOI: **10.1016/j.aca.2016.08.010**.

39 Z. Masoumi, M. Tayebi and B.-K. Lee, Ultrasonication-Assisted Liquid-Phase Exfoliation Enhances Photoelectrochemical Performance in α-Fe$_2$O$_3$/MoS$_2$ Photoanode, *Ultrason. Sonochem.*, 2021, **72**, 105403, DOI: **10.1016/j.ultsonch.2020.105403**.

40 S. Ghayeb, R. Karimzadeh and S. H. Aboutalebi, Laser-Assisted Tunable Optical Nonlinearity in Liquid-Phase Exfoliated MoS$_2$ Dispersion, *Appl. Phys. A: Mater. Sci. Process.*, 2018, **124**, DOI: **10.1007/s00339-018-2115-2**.

41 A. Castellanos-Gomez, J. Quereda, H. P. Meulen, N. van der; Agraït and G. Rubio-Bollinger, Spatially Resolved Optical Absorption Spectroscopy of Single- and Few-Layer MoS$_2$ by Hyperspectral Imaging, *Nanotechnology*, 2016, **27**(11), 115705, DOI: **10.1088/0957-4484/27/11/115705**.

42 C. Backes, R. J. Smith, N. McEvoy, N. C. Berner, D. McCloskey, H. C. Nerl, A. O'Neill, P. J. King, T. Higgins, D. Hanlon, N. Scheuschner, J. Maultzsch, L. Houben, G. S. Duesberg, J. F. Donegan, V. Nicolosi and J. N. Coleman, Edge and Confinement Effects Allow in Situ Measurement of Size and Thickness of Liquid-Exfoliated Nanosheets, *Nat. Commun.*, 2014, **5**, 4576, DOI: **10.1038/ncomms5576**.

43 C. Backes, T. M. Higgins, A. Kelly, C. Boland, A. Harvey, D. Hanlon and J. N. Coleman, Guidelines for Exfoliation, Characterization and Processing of Layered Materials Produced by Liquid Exfoliation, *Chem. Mater.*, 2017, **29**(1), 243–255, DOI: **10.1021/acs.chemmater.6b03335**.

44 E. Varrla, C. Backes, K. R. Paton, A. Harvey, Z. Gholamvand, J. McCauley and J. N. Coleman, Large-Scale Production of Size-Controlled MoS$_2$ Nanosheets by Shear Exfoliation, *Chem. Mater.*, 2015, **27**(3), 1129–1139, DOI: **10.1021/cm5044864**.

45 X. Jiang, Y. Sun, H. Zhang and L. Hou, Preparation and Characterization of Quaternized Poly(Vinyl Alcohol)/Chitosan/MoS$_2$ Composite Anion Exchange Membranes with High Selectivity, *Carbohydr. Polym.*, 2018, **180**, 96–103, DOI: **10.1016/j.carbpol.2017.10.023**.

46 S. Han, K. Liu, L. Hu, F. Teng, P. Yu and Y. Zhu, Superior Adsorption and Regenerable Dye Adsorbent Based on Flower-Like Molybdenum Disulfide Nanostructure, *Sci. Rep.*, 2017, **7**(1), 43599, DOI: **10.1038/srep43599**.

47 N. Hussain, M. A. Abdelkareem, H. Alawadhi, A. H. Alami and K. Elsaid, Cu$_2$O Nanoparticles Decorated with MoS$_2$ Sheets for Electrochemical Reduction of CO$_2$ with Enhanced Efficiency, *Appl. Phys. A: Mater. Sci. Process.*, 2022, **128**(2), 131, DOI: **10.1007/s00339-021-05230-0**.

48 A. Abareshi, R. Bafkari, M. Houshiar and R. Dinarvand, Molybdenum Disulfide/Carbon Nanocomposite with Enhanced Photothermal Effect for Doxorubicin Delivery, *Eur. Phys. J. Plus*, 2021, **136**(1), 57, DOI: **10.1140/epjp/s13360-020-01022-2**.

49 K.-J. Huang, Y.-J. Liu, Y.-M. Liu and L.-L. Wang, Molybdenum Disulfide Nanoflower-Chitosan–Au Nanoparticles Composites Based Electrochemical Sensing Platform for Bisphenol A Determination, *J. Hazard. Mater.*, 2014, **276**, 207–215, DOI: **10.1016/j.jhazmat.2014.05.037**.

50 R. Zribi, A. Foti, M. G. Donato, P. G. Gucciardi and G. Neri, Fabrication of a Novel Electrochemical Sensor Based on Carbon Cloth Matrix Functionalized with MoO$_3$ and 2D-MoS$_2$ Layers for Riboflavin Determination, *Sensors*, 2021, **21**(4), 1371, DOI: **10.3390/s21041371**.

51 G. P. Mikhailov, S. V. Tuchkov, V. V. Lazarev and E. I. Kulish, Complexation of Chitosan with Acetic Acid According to Fourier Transform Raman Spectroscopy Data, *Russ. J. Phys. Chem. A*, 2014, **88**(6), 936–941, DOI: **10.1134/S0036024414060181**.

52 W. Yin, L. Yan, J. Yu, G. Tian, L. Zhou, X. Zheng, X. Zhang, Y. Yong, J. Li, Z. Gu and Y. Zhao, High-throughput synthesis of single-layer MoS$_2$ nanosheets as a near-infrared photothermal-triggered drug delivery for effective cancer therapy, *ACS Nano*, 2014, **8**(7), 6922–6933.

53 R. Zribi, A. Foti, M. G. Donato, P. G. Gucciardi and G. Neri, Electrochemical and Sensing Properties of 2D-MoS$_2$ Nanosheets Produced via Liquid Cascade Centrifugation, *Electrochim. Acta*, 2022, **436**, 141433, DOI: **10.1016/j.electacta.2022.141433**.

54 N. O. Laschuk, E. B. Easton and O. V. Zenkina, Reducing the Resistance for the Use of Electrochemical Impedance Spectroscopy Analysis in Materials Chemistry, *RSC Adv.*, 2021, **11**(45), 27925–27936, DOI: **10.1039/D1RA03785D**.

55 B.-A. Mei, O. Munteshari, J. Lau, B. Dunn and L. Pilon, Physical Interpretations of Nyquist Plots for EDLC Electrodes and Devices, *J. Phys. Chem. C*, 2018, **122**(1), 194–206, DOI: **10.1021/acs.jpcc.7b10582**.

56 M. R. Islam, Homaira, E. Mahmud and R. B. Alam, MoS$_2$ Nanoflower Decorated Bio-Derived Chitosan Nanocomposites for Sustainable Energy Storage: Structural, Optical and Electrochemical Studies, *Heliyon*, 2024, **10**(3), DOI: **10.1016/j.heliyon.2024.e25424**.

57 R. Ke, X. Zhang, L. Wang, C. Zhang, S. Zhang, H. Niu, C. Mao, J. Song, B. Jin and Y. Tian, Enhanced Electrochemiluminescence of CdSe Quantum Dots Coupled with MoS$_2$–Chitosan Nanosheets, *J. Solid State Electrochem.*, 2015, **19**(6), 1633–1641, DOI: **10.1007/s10008-015-2793-z**.

58 S. E. Elugoke, O. E. Fayemi, A. S. Adekunle, F. A. Adesanya and E. E. Ebenso, Electrochemical Detection of Dopamine at a Novel Poly(2,4,6-Trihydroxybenzaldehyde) Film Modified Electrode, *ChemElectroChem*, 2024, **11**(7), e202400021, DOI: **10.1002/celc.202400021**.

59 M. Sajid, M. K. Nazal, M. Mansha, A. Alsharaa, S. M. S. Jillani and C. Basheer, Chemically Modified Electrodes for Electrochemical Detection of Dopamine in the Presence of Uric Acid and Ascorbic Acid: A Review, *TrAC, Trends Anal. Chem.*, 2016, **76**, 15–29, DOI: **10.1016/j.trac.2015.09.006**.

60 A. N. Patel, S. Tan, T. S. Miller, J. V. Macpherson and P. R. Unwin, Comparison and Reappraisal of Carbon Electrodes for the Voltammetric Detection of Dopamine, *Anal. Chem.*, 2013, **85**(24), 11755–11764, DOI: **10.1021/ac401969q**.

61 M. N. Ranku, G. E. Uwaya and O. E. Fayemi, Electrochemical Detection of Dopamine at Fe$_3$O$_4$/SPEEK Modified Electrode, *Molecules*, 2021, **26**(17), 5357, DOI: **10.3390/molecules26175357**.

62 G. Xu, Z. A. Jarjes, V. Desprez, P. A. Kilmartin and J. Travas-Sejdic, Sensitive, Selective, Disposable Electrochemical Dopamine Sensor Based on PEDOT-Modified Laser Scribed Graphene, *Biosens. Bioelectron.*, 2018, **107**, 184–191, DOI: **10.1016/j.bios.2018.02.031**.

63 C. Wang, J. Du, H. Wang, C. Zou, F. Jiang, P. Yang and Y. Du, A Facile Electrochemical Sensor Based on Reduced Graphene Oxide and Au Nanoplates Modified Glassy Carbon Electrode for Simultaneous Detection of Ascorbic Acid, Dopamine and Uric Acid, *Sens. Actuators, B*, 2014, **204**, 302–309, DOI: **10.1016/j.snb.2014.07.077**.

64 D.-S. Kim, E.-S. Kang, S. Baek, S.-S. Choo, Y.-H. Chung, D. Lee, J. Min and T.-H. Kim, Electrochemical Detection of Dopamine Using Periodic Cylindrical Gold Nanoelectrode Arrays, *Sci. Rep.*, 2018, **8**(1), 14049, DOI: **10.1038/s41598-018-32477-0**.

65 R. Zribi, R. Maalej, R. Gillibert, M. G. Donato, P. G. Gucciardi, S. G. Leonardi and G. Neri, Simultaneous and Selective Determination of Dopamine and Tyrosine in the Presence of Uric Acid with 2D-MoS$_2$ Nanosheets Modified Screen-Printed Carbon Electrodes, *FlatChem*, 2020, **24**, 100187, DOI: **10.1016/j.flatc.2020.100187**.

66 I. Anshori, R. R. Althof, L. N. Rizalputri, E. Ariasena, M. Handayani, A. Pradana, M. R. Akbar, M. R. A. A. Syamsunarno, A. Purwidyantri, B. A. Prabowo, M. S. Annas, H. Munawar and B. Yuliarto, Gold Nanospikes Formation on Screen-Printed Carbon Electrode through Electrodeposition Method for Non-Enzymatic Electrochemical Sensor, *Metals*, 2022, **12**(12), 2116, DOI: **10.3390/met12122116**.

67 T. Guinovart, D. Hernández-Alonso, L. Adriaenssens, P. Blondeau, F. X. Rius, P. Ballester and F. J. Andrade, Characterization of a New Ionophore-Based Ion-Selective Electrode for the Potentiometric Determination of Creatinine in Urine, *Biosens. Bioelectron.*, 2017, **87**, 587–592, DOI: **10.1016/j.bios.2016.08.025**.

68 Y. Haldorai, A. T. E. Vilian, M. Rethinasabapathy, Y. S. Huh and Y.-K. Han, Electrochemical Determination of Dopamine Using a Glassy Carbon Electrode Modified with TiN-Reduced Graphene Oxide Nanocomposite, *Sens. Actuators, B*, 2017, **247**, 61–69, DOI: **10.1016/j.snb.2017.02.181**.